Supporting Information

Multilevel, solar-blind and thermostable physical unclonable functions based on host-sensitized luminescence of β-Ga_2O_3:Dy^{3+}

Dong Zhu,[1,2] Chunfeng Wang,[1*] Fuhang Jiao,[1] Jiujun Xu,[1] Haoran Xu,[1] Shun Han,[1] Peijiang Cao,[1] Yuxiang Zeng,[1] Ming Fang,[1] Wenjun Liu,[1] Deliang Zhu,[1 *] and Youming Lu,[1,2 *]

1 College of Materials Science and Engineering, Guangdong Research Center for Interfacial Engineering of Functional Materials, Shenzhen University, Shenzhen 518060, PR China.

2 College of Physics and Optoelectronic Engineering Shenzhen University, Shenzhen 518060, China.

*E-mail: ymlu@szu.edu.cn (Youming Lu); cfwang@szu.edu.cn (Chunfeng Wang); dlzhu@szu.edu.cn (Delang Zhu)

The supporting information including:

Supplementary note S1-S4

Supplementary figures S1-S10

Supplementary table S1-S5

Note S1†

Determining the quenching concentration of rare earth ions is crucial for identifying the optimal doping level to achieve the highest luminescence efficiency. Investigating the quenching mechanisms provides insights into the luminescence mechanisms of phosphors, including the processes of energy transfer and the pathways of electron transitions. By analyzing the relationship between the PL intensity and concentration of β-Ga_2O_3:xDy^{3+} phosphors ($1 \leq x \leq 0.05$, $\Delta x = 0.01$), the **quenching concentration** (*QC*) [1]

$$I = Bc(1-c)^z$$

$$QC = \frac{1}{1+z}$$

where *B* is a constant, *c* is the molar fraction of the activator ions, and *I* is the luminescence intensity, QC~3.01%, which was in good agreement with experimental findings. The **quenching mechanisms** [2]

$$\log\left(\frac{I}{c}\right) = \left(\frac{-s}{d}\right) \times \log c + \log f$$

Where *I* represents the luminescence intensity; *c* represents the concentration of activator ions; *s* represents the interaction constant; *d* represents the dimensionality of the sample, with *d*=3 for particulate samples; *f* is a constant. The resulting slopes, −0.83 and −0.84, are both close to −1, indicating that *s* is approximately equal to 3, which attributed to dipole-dipole interactions (d-d). This interaction involves the energy transfer between the d electrons of rare earth ions. As the doping concentration of Dy^{3+} increases, the distance between adjacent ions decreases, enhancing the d-d and consequently promoting non-radiative energy dissipation from the excited state, which reduces PL intensity. This mechanism is generally not significantly temperature-dependent, as it is primarily determined by the arrangement of ions and the strength of their interactions. However, it can be influenced by defect energy levels within the matrix, which can act as traps or recombination centers for energy migration, thereby affecting

the efficiency and path of energy transfer[3]. This understanding offers a theoretical foundation for modulating the luminescence of Dy^{3+} by tailoring the defects in β-Ga_2O_3.

Note S2†

Quantum efficiency (*QE*) is a crucial indicator for assessing the quality of phosphors. It refers to the ratio of the number of photons absorbed by the phosphor to the number of photons emitted, directly reflecting the phosphor's ability to convert absorbed energy into light emission efficiency. A high quantum efficiency implies that the phosphor can more effectively convert the excitation energy into light output [4].

$$QE = \frac{\int L_s}{\int E_r - \int E_s}$$

where L_s represents the emission spectrum of the phosphor, E_r represents the spectrum of the excitation light from the xenon lamp, and E_s represents the spectrum of the excitation light reflected from the sample.

QE of β-Ga_2O_3:Dy is significantly higher than its intrinsic luminescence, as shown in **Table S3**, indicating that the energy transfer efficiency from the matrix to Dy^{3+} ions is very high.

Note S3†.

Colour Temperature (*T*)

The colour coordinates provide an accurate way to describe and distinguish the colour of light emitted by phosphors, while the **colour temperature** (*T*) assists in distinguishing the consistency of the colour of light emitted by different phosphors or by the same phosphor under different conditions. The T for each sample is determined according to the equation[5]

$$n = \frac{x - 0.332}{y - 0.1858}$$

$$T = -437n^3 + 3601n^2 - 6861n + 5514.31$$

where the *x* and *y* values represent the CIE coordinates and are detailed in **Table S4**.

Note S4†

The activation energy for thermal quenching (E_a) is a key parameter for measuring the thermal stability of phosphors. A high activation energy implies that the phosphor can maintain good luminescent performance at high temperatures because more energy is required for the luminescence process to be thermally affected. The Arrhenius equation describes the relationship between the luminescence intensity of phosphors and temperature changes. By calculating the activation energy, the performance of phosphors at different temperatures can be predicted, which is crucial for designing devices that operate within a specific temperature range.

E_a is defined as energy necessary for an excited electron to overcome potential barrier and transition to other levels [6]

$$I_T = I_0 \times e^{-\frac{E_a}{kT}}$$

where, k is the Boltzmann's constant (8.617105×10^{-5} eV/K), I_T and I_0 stand for the luminous intensity at target temperature and room temperature separately.

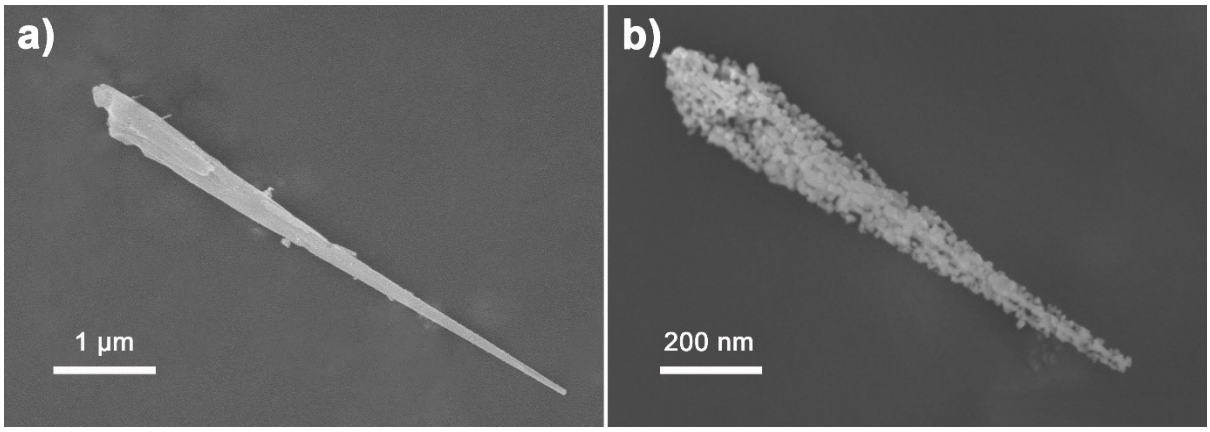

Fig. S1†. FE-SEM images of a single β-Ga_2O_3 nanorod precursor (a) and the same nanorod after calcination at 950°C (b), showing significant morphological changes due to thermal treatment.

The GaOOH precursors showed a typical rod morphology, grown from a broader base and tapering at the tip, with a smooth and homogeneous surface, which was attributed to the slow stirring in a constant pH environment, which gave stable nucleation conditions for the six-directional GaOOH. The rod structure of the precursor was not destroyed because of the addition of n-hexane during the cleaning process, whereas the lower drying temperature retained a trace amount of bound water in the precursor, and the suitable rate of warming resulted in the agglomeration of β-Ga_2O_3 as particles into a rod-like morphology.

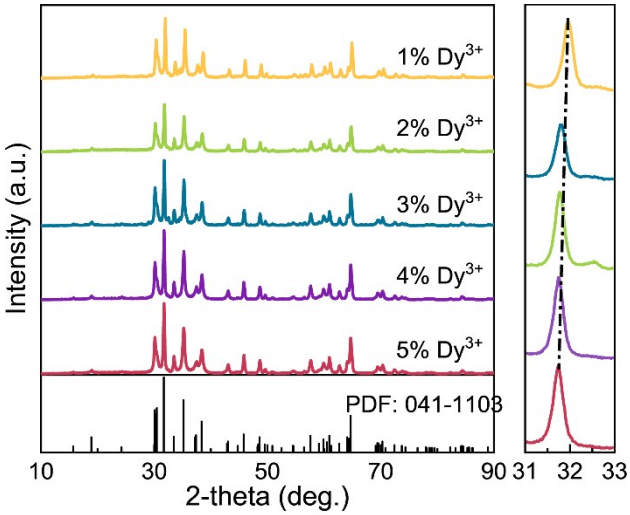

Fig. S2†. XRD patterns of β-Ga_2O_3 doped with varying concentrations of Dy^{3+} ions. The inset highlights the detailed enlargement of the (111) diffraction peak, illustrating shifts and intensity variations related to Dy^{3+} doping levels.

The small ionic radius of Ga is replaced by the large size of Dy and the lattice undergoes expansion, which causes the XRD shifted to a large angle.

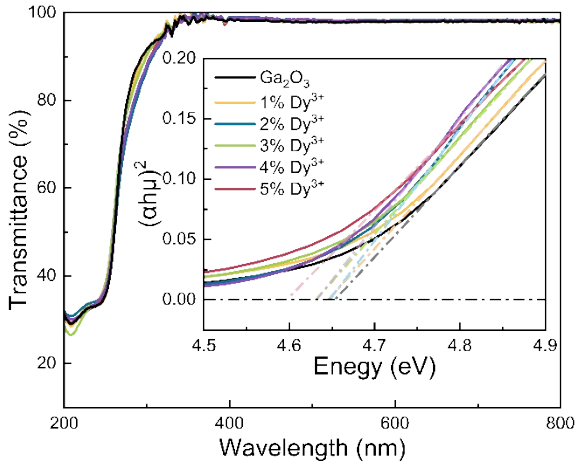

Fig. S3†. Ultraviolet-visible light transmission spectra of β-Ga_2O_3:xDy^{3+} phosphors ($0 \leq x \leq 0.05$, $\Delta x = 0.01$), with the inset showing the Tauc plot of $(\alpha h\nu)^2$ versus photon energy (eV).

With increasing Dy^{3+} concentration, the absorption edge shifts towards the long-wavelength side, indicating a narrowing of the optical bandgap. According to the following formula:[7]

$$(\alpha h\nu)^2 = A(h\nu - Eg)$$

$$\alpha = \frac{ln\left(\frac{1}{T}\right)}{d}$$

where the symbol $h\nu$ signifies the energy of a photon, the absorption coefficient is denoted by α, which is calculated on the basis of the transmittance T and the thickness d of the powdered material; here, A, T and d are considered constants for this particular computation. The undoped β-Ga_2O_3 has an optical bandgap of approximately 4.6 eV. Intriguingly, with increasing Dy^{3+} doping level, a progressive reduction in the optical bandgap of the β-Ga_2O_3:Dy^{3+} nanorods is observed. This downwards trend is graphically depicted in the inset of **Figure S3**, which provides a clear visual representation of the phenomenon. The underlying mechanism for this bandgap narrowing is rooted in the increased incorporation of defects into the host crystal lattice with increasing Dy^{3+} ion concentration. The introduction of these defects disrupts the

periodic potential of the host material, which in turn affects the electronic structure and leads to a decrease in the bandgap energy.[8]

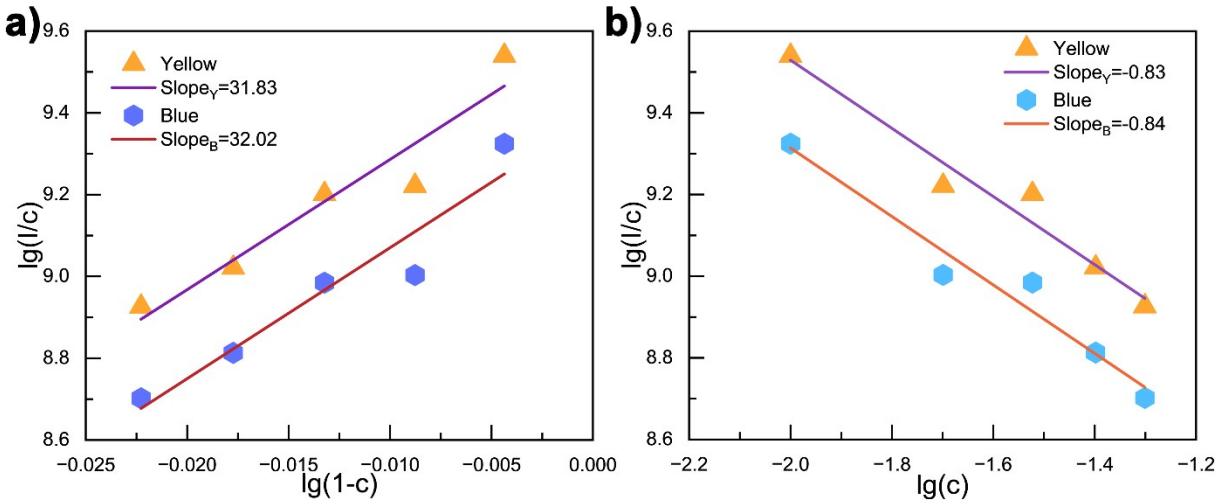

Fig. S4†. Quenching concentration (a) and quenching mechanism (b) of β-Ga_2O_3:xDy^{3+} (0.01 ≤ x ≤ 0.05, Δx = 0.01) phosphors with varying Dy^{3+} concentrations.

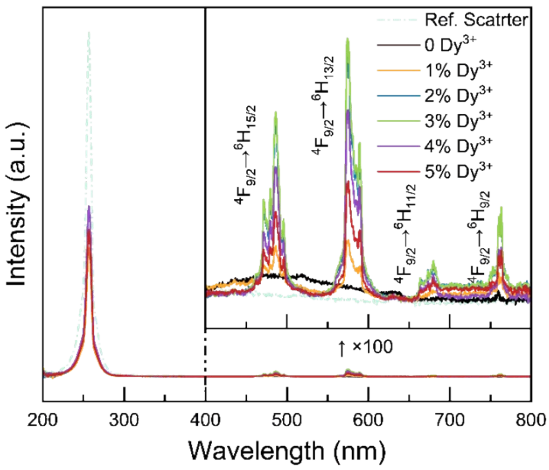

Fig. S5†. QE of β-Ga_2O_3:xDy^{3+} phosphors at various Dy^{3+} concentrations ($0 \leq x \leq 0.05$, $\Delta x = 0.01$)

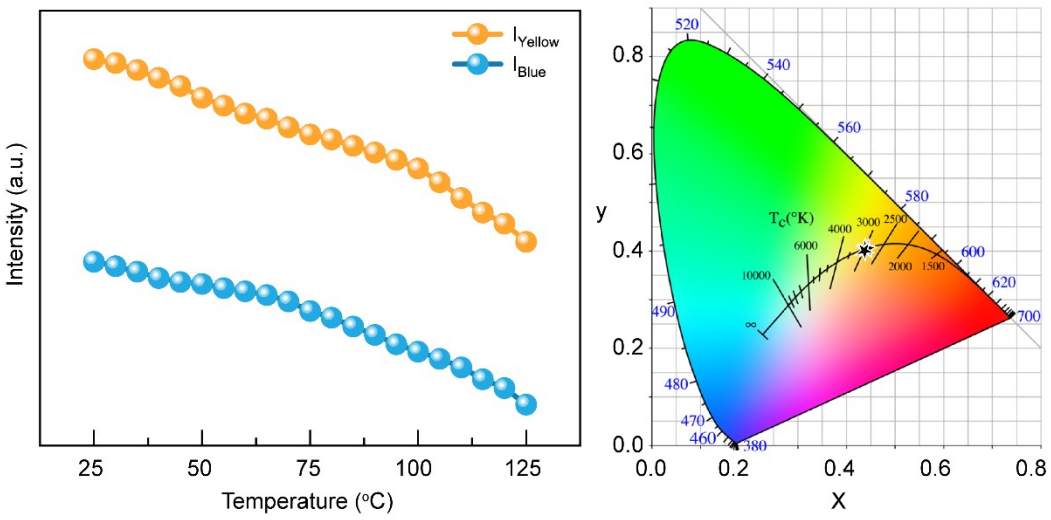

Fig. S6† Temperature-dependent PL spectra of β-Ga_2O_3:3%Dy^{3+} phosphors, comparing the intensity of dual emission peaks (a), with corresponding CIE chromaticity coordinates (b) and correlated color temperature (CCT) values (refer to Table 4), indicating thermal stability and color consistency**.**

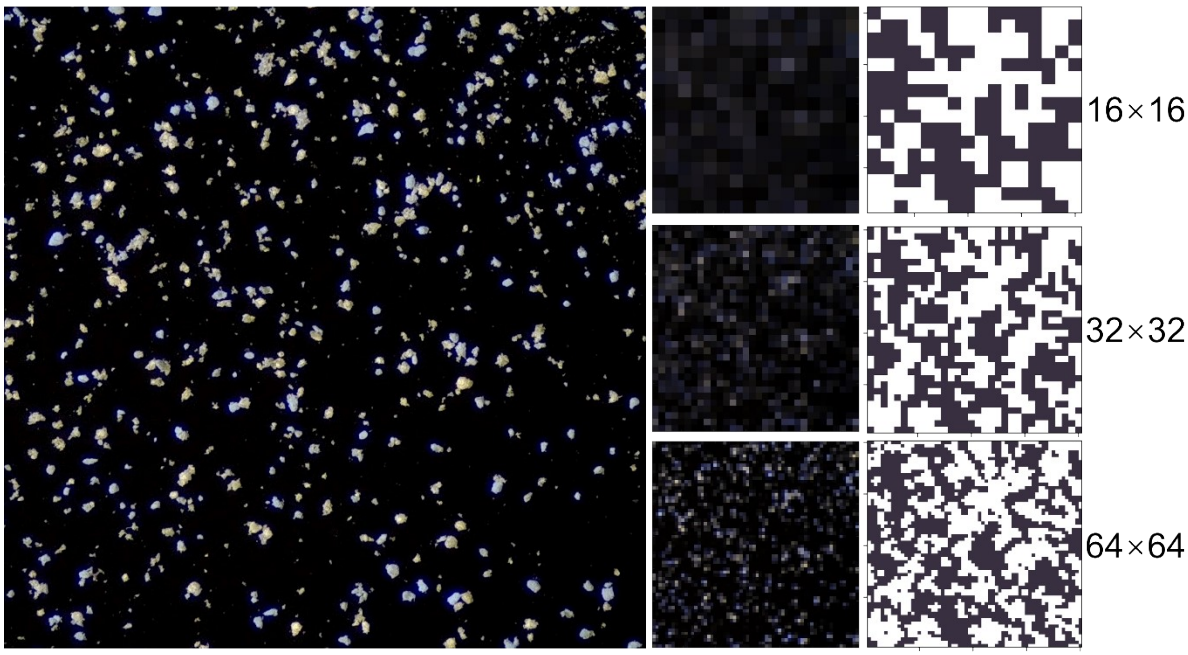

Fig. S7† The process of generating bitmaps of different sizes from the same PUF Tag.

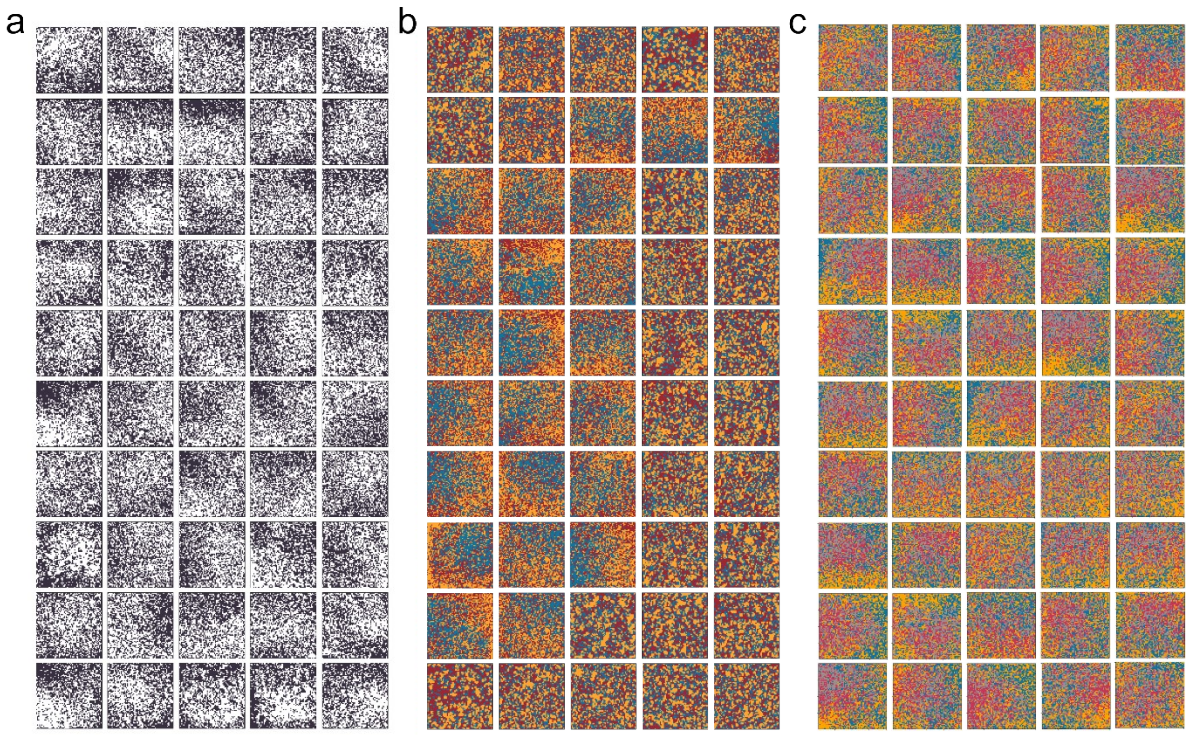

Fig. S8† The bitmaps of binary (a), trinary (b) and quadratic (c) generated from 50 different images, respectively.

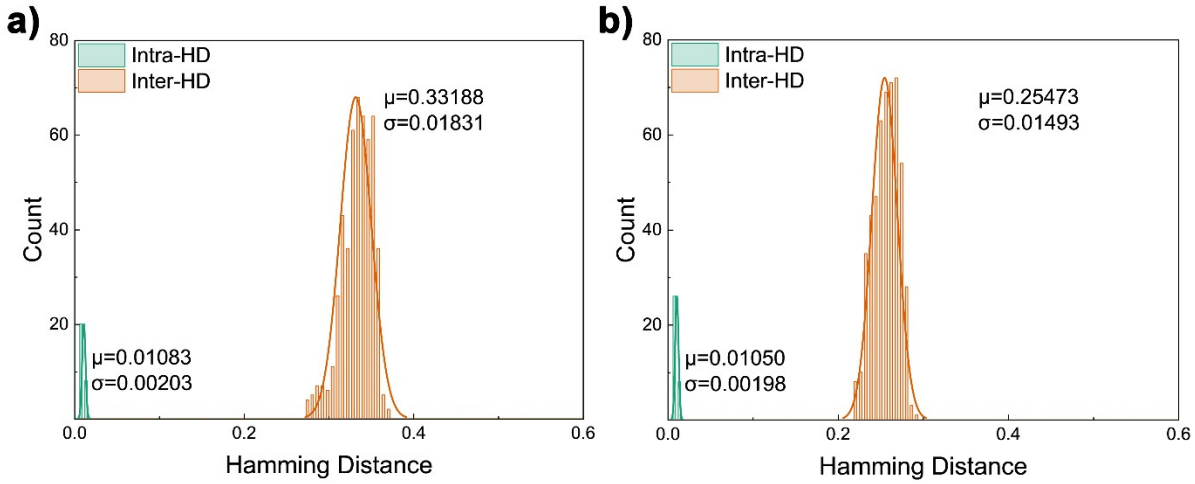

Fig. S9†. Statistical distribution of inter-device Hamming distances (HDs) and intra-device HDs calculated for trinary (a) and quadratic (b) bitmaps from 50 different PUF labels.

The Hamming distance is the number of different characters in the same position between two equal-length strings. Binary codes have a relatively simple structure and usually contain a large amount of binary information, so the use of the Hamming distance allows for quick and effective evaluation and comparison of the similarity of these binary data. The correlation coefficient measures the degree of linear correlation between two variables. In multidimensional codes, where the codes may contain more complex data structures and types, correlation coefficients allow for a more comprehensive assessment of similarity and variation between codes.[9]

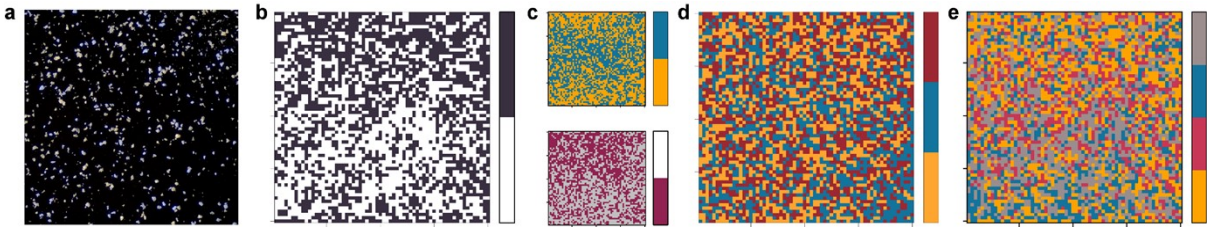

Fig. S10†. Fabrication process of multi-level PUF. (a) Optical image of the PUF tag. (b) Binary bitmap generated from the optical image. (c) Different bitmaps generated by dividing the thresholds based on different color channels. (d) Ternary bitmap generated from the optical image. (e) Quaternary bitmap generated from the optical image.

Table S1† Refined crystal structure information of β-Ga_2O_3:3%Dy^{3+} at room temperature (25°C).

Space group	C2/m						
Chemical Formula	Theory				This Work		
Structural Density (g/cm^3)	5.94				7.062		
a (Å)	12.230				12.2798692		
b (Å)	3.040				3.0330350		
c (Å)	5.800				5.8033988		
β (∘)	103.70				103.7927		
V(Å^3)	209.50				209.91796		
Rwp	5.13%						
	Atomic Coordinate						
	x(Å)		y(Å)		z(Å)		Occ.
Site	Theory	This	Theor	This	Theory	This	
Ga_I	0.0904	0.09331	0	0	0.2948	0.79767	95.760
Dy_I							4.240%
Ga_{II}	0.3414	0.15964	0.5	0.5	0.1857	0.3199	98.757
Dy_{II}							1.243%
O_I	0.0043	0.00095	0.5	0.5	0.7447	0.73641	100%
O_{II}	0.1640	0.16391	0	0	0.1507	0.15085	100%
O_{III}	0.1674	0.16527	0	0	0.6011	0.63921	100%

As shown in the table, 4.240% of the Ga positions of the octahedra were replaced by Dy, 1.243% of the Ga lattice positions of the tetrahedra were replaced by Dy, and the doped Dy accounted for 2.7415% of all Ga, which is close to the experimental value of 3%.

Table S2†. Comparison of experimental Raman-active modes for β-Ga_2O_3:3%Dy^{3+} with standard theory[10] for undoped β-Ga_2O_3

	Phonon mode	This Work	Theory	Assignments
The low-frequency modes	$Ag^{(1)}$	110.89	111.0	Translation-liberation of tetrahedron-
	$Bg^{(1)}$	113.36	114.8	
	$Bg^{(2)}$	144.25	144.8	
	$Ag^{(2)}$	168.87	169.9	
	$Ag^{(3)}$	199.55	200.2	
The mid-frequency modes	$Ag^{(4)}$	319.86	230.0	Deformation of GaO_6 octahedron
	$Ag^{(5)}$	347.56	346.6	
	$Bg^{(3)}$	358.78	356.0	
	$Ag^{(6)}$	415.77	416.2	
	$Ag^{(7)}$	475.07	474.9	
	$Bg^{(4)}$	480.91	474.9	
The high-frequency modes	$Ag^{(8)}$	629.7	630.0	Stretching and bending vibration of
	$Bg^{(5)}$	651.70	652.3	
	$Ag^{(9)}$	657.4	658.3	
	$Ag^{(10)}$	767.58	766.7	

The peak positions of β-Ga_2O_3:3%Dy^{3+} compared to the theoretical pure-phase β-Ga_2O_3 were basically the same and no new phonon vibrational modes emerged.

Table S3†. QE of β-Ga_2O_3:xDy^{3+} phosphors at various Dy^{3+} concentrations ($0 \leq x \leq 0.05$, $\Delta x = 0.01$)

Dy (%)	QE (%)
0	13.26
1	18.95
2	31.09
3	36.57
4	26.58
5	24.71

Table S4†. Colour temperature statistics of different samples

Sample	CIE	Colour
S1	(0.4459, 0.4068)	2874
S2	(0.3928, 0.3853)	3745
S3	(0.3754, 0.3733)	4114
S4	(0.3559, 0.3635)	4656
S5	(0.2769, 0.2910)	10159

Table S5†. Colour temperature statistics of different samples

Temperature (°C)	CIE x	CIE y	Peak	T
25	0.4459	0.4068	581	2874
30	0.4490	0.4118	581	2866
35	0.4482	0.4110	581	2872
40	0.4488	0.4122	581	2873
45	0.4477	0.4107	581	2878
50	0.4474	0.4105	581	2881
55	0.4457	0.4084	581	2891
60	0.4473	0.4118	581	2893
65	0.4457	0.4089	581	2895
70	0.4457	0.4103	581	2906
75	0.4459	0.4119	581	2915
80	0.4448	0.4109	581	2925
85	0.4442	0.4100	581	2927
90	0.4439	0.4103	581	2935
95	0.4440	0.4106	581	2935
100	0.4439	0.4106	581	2937
105	0.4428	0.4095	581	2946
110	0.4414	0.4086	581	2961
115	0.4410	0.4079	581	2962
120	0.4391	0.4056	581	2975
125	0.4387	0.4066	581	2990

As the temperature increased from 25°C to 125°C, the yellow/blue light intensity of both β-Ga_2O_3:3%Dy^{3+} phosphors decreased, but the colour coordinates remained essentially unchanged, and the colour temperature increased slightly by ~4%, with insignificant differences.

References

1. S. Devi, V. Taxak and S. Khatkar, *Chem. Phys. Lett.*, 2021, **765**, 138289.

2. W. B. Dai, Y. M. Fan, M. Xu and F. Shen, *J. Appl. Phys.*, 2021, **129**, 093101.

3. H. C. Sun, Q. Yang, J. L. Wang, M. C. Ding, M. Y. Cheng, L. Liao, C. Cai, Z. T. Chen, X. D. Huang Z. B. Wang, Z. Xu, W. L. Wang, K. H. Liu, L. Liu, X. D. Bai, J. Chen, S. Meng and L. F. Wang, *Nat. Commun.*, 2024, 15, 9476.

4. X. Li, D. Wang, Y. Zhong, F. Jiang, D. Zhao, S. Sun, P. Lu, M. Lu, Z. Wang, Z. Wu, Y. Gao, Y. Zhang, W. Yu and X. Bai, *Adv. Sci.*, 2023, **10**, 2207571.

5. J. R. Jose, T. A. Jose, A. J. Ashok, C. Joseph and P. Biju, *J. Alloy. Compd.*, 2024, **1006**, 176304.

6. A. Bindhu, J. I. Naseemabeevi and S. Ganesanpotti, *Dalton T.*, 2023, **52**, 11705-11715.

7. A. Gopinath, S. A. Oommen, A. J. Ashok, C. Joseph and P. Biju, *Mat. Sci. Semicon. Porc.*, 2025, **185**, 108875.

8. F. Liu and Z. X. Fan, *Chem. Soc. Rev.*, 2023, **52**, 1723-1772.

9. A. K. Varshney, P. K. Muhuri and Q. M. D. Lohani, *Appl. Soft Comput*., 2022, **120**, 108584.

10. J. S. Wei, Y. Z. Bu, Q. L. Sai, H. J. Qi, J. B. Li and H. M. Gu, *Cryst. Eng. Comm.*, 2023, **25**, 4317-4324.